Monthly Notices of the ROYAL ASTRONOMICAL SOCIETY

MNRAS **496,** 3412–3423 (2020)
Advance Access publication 2020 June 13

doi:10.1093/mnras/staa1683

The lively accretion disc in NGC 2992 – I. Transient iron K emission lines in the high-flux state

A. Marinucci,[1★] S. Bianchi,[2] V. Braito,[3,4] B. De Marco,[5] G. Matt,[2] R. Middei,[6,7] E. Nardini[8,9] and J. N. Reeves[3,4]

[1]*ASI – Unità di Ricerca Scientifica, Via del Politecnico snc, I-00133 Roma, Italy*
[2]*Dipartimento di Matematica e Fisica, Università degli Studi Roma Tre, Via della Vasca Navale 84, I-00146 Roma, Italy*
[3]*Center for Space Science and Technology, University of Maryland Baltimore County, 1000 Hilltop Circle, Baltimore, MD 21250, USA*
[4]*INAF – Osservatorio Astronomico di Brera, Via Bianchi 46, I-23807 Merate (LC), Italy*
[5]*Nicolaus Copernicus Astronomical Center, Polish Academy of Sciences, Bartycka 18, PL-00-716 Warsaw, Poland*
[6]*INAF – Osservatorio Astronomico di Roma, Via Frascati 33, I-00078 Monte Porzio Catone (RM), Italy*
[7]*ASI – Space Science Data Center, Via del Politecnico snc, I-00133 Roma, Italy*
[8]*Dipartimento di Fisica e Astronomia, Università di Firenze, via G. Sansone 1, I-50019 Sesto Fiorentino (FI), Italy*
[9]*INAF – Osservatorio Astrofisico di Arcetri, Largo Enrico Fermi 5, I-50125 Firenze, Italy*

Accepted 2020 June 8. Received 2020 June 4; in original form 2020 April 14

ABSTRACT

We report on one of the brightest flux levels of the Seyfert 2 galaxy NGC 2992 ever observed in X-rays, on 2019 May. The source has been monitored every few days from 2019 March 26 to 2019 December 14 by *Swift*-X-Ray Telescope (XRT), and simultaneous *XMM–Newton* (250 ks) and *NuSTAR* (120 ks) observations were triggered on 2019 May 6. The high count rate of the source (its 2–10 keV flux ranged between 0.7 and 1.0×10^{-10} erg cm^{-2} s^{-1}) allows us to perform a time-resolved spectroscopy, probing spatial scales of tens of gravitational radii from the central black hole. By constructing a map of the excess emission over the primary continuum, we find several emission structures in the 5.0–7.2 keV energy band. From fitting the 50 European Photon Imaging Camera (EPIC)-pn spectral slices of ∼5 ks duration, we interpret them as a constant narrow iron Kα line and three variable components in the iron K complex. When a self-consistent model accounting for the accretion disc emission is considered (KYNRLINE), two of these features (in the 5.0–5.8 and 6.8–7.2 keV bands) can be ascribed to a flaring region of the accretion disc located at $r_{\rm in} \simeq 15$–$40r_{\rm g}$ from the black hole. The third one (6.5–6.8 keV) is likely produced at much larger radii ($r_{\rm in} > 50r_{\rm g}$). The inner radius and the azimuthal extension retrieved from the co-added spectra of the flaring states are $r_{\rm in} = 15 \pm 3r_{\rm g}$ and $\phi = 165°$–$330°$, suggesting that the emitting region responsible for the broad iron K component is a relatively compact annular sector within the disc. Our findings support a physical scenario in which the accretion disc in NGC 2992 becomes more active at high accretion rates ($L_{\rm bol}/L_{\rm Edd} \geq 4$ per cent).

Key words: accretion, accretion discs – galaxies: active – galaxies: individual: NGC 2992 – galaxies: Seyfert.

1 INTRODUCTION

Active galactic nuclei (AGN) that show high X-ray variability on relatively short (less than hundreds of ks) time-scales are the perfect astrophysical laboratories for studying the response of the accretion disc to changes of the primary continuum. Spectral features both in emission and in absorption have been detected in bright sources and can be studied to infer the physical properties of the circumnuclear matter (MCG–6-30-15, IRAS 13224−3809; Iwasawa et al. 1999; Fabian & Vaughan 2003; Marinucci et al. 2014; Parker et al., 2017a,b). On the other hand, the reverberation of the X-ray radiation reprocessed by the accretion disc (De Marco et al. 2013; Uttley et al. 2014; Kara et al. 2016) suggests that the hot corona, responsible for the primary continuum, has a typical size of a few gravitational radii and is located close to the central supermassive black hole (SMBH). This is also supported by microlensing experiments on quasars (Chartas et al. 2009; Guerras et al. 2017).

A narrow neutral iron Kα emission line at 6.4 keV is ubiquitous in nearby AGN (George et al. 2000; Perola et al. 2002; Bianchi et al. 2007) and when a broad component is detected, this is indicative of special and general relativistic effects (Nandra et al.

★ E-mail: andrea.marinucci@asi.it

1997; Fabian et al. 2000; Reynolds & Nowak 2003) occurring at a few gravitational radii $r_g = GM/c^2$ from the central SMBH. Many studies on the variability pattern of such a broad iron Kα component have been presented in the past (Iwasawa, Miniutti & Fabian 2004; Longinotti et al. 2004; Turner et al. 2006; Petrucci et al. 2007; Tombesi et al. 2007; De Marco et al. 2009; Nardini et al. 2016), typically on time-scales of tens of ks.

NGC 2992 is a nearby ($z = 0.00771$; Keel 1996) Seyfert 1.9/1.5 galaxy (Trippe et al. 2008). In X-rays, it is absorbed by a column density $N_H \sim 9 \times 10^{21}$ cm^{-2} and it has been observed to vary in flux by up to a factor of 20 in a few years, and by almost an order of magnitude on time-scales of days (0.8–8.9 $\times 10^{-11}$ erg cm^{-2} s^{-1}; Murphy, Yaqoob & Terashima 2007). Even though the source has been extensively observed by all major X-ray satellites, its high flux level is still poorly studied. The time variability of the iron Kα line is intriguing, suggesting the presence of a broad iron Kα component, between 5 and 6 keV, which becomes more intense at high flux levels (Yaqoob et al. 2007; Shu et al. 2010; Marinucci et al. 2018). This is the opposite of what is usually observed in other bright sources with relativistic lines and explained in the framework of the light bending model (Martocchia & Matt 1996; Miniutti & Fabian 2004).

We hereby present results from the *XMM–Newton* and *NuSTAR* observations of a high flux level of NGC 2992 occurred in 2019 May ($F_{2-10} > 7 \times 10^{-11}$ erg cm^{-2} s^{-1}), with the aim of constraining the Fe K line emission regions, by monitoring the variability patterns of the line. The paper is structured as follows. In Section 2, we discuss the observations and data reduction. In Section 3, we present the iron K excess map, the excess variance F_{var} spectrum, and the spectral analyses. We discuss and summarize the physical implications of our results in Sections 4 and 5.

2 OBSERVATIONS AND DATA REDUCTION

2.1 *Swift*

The past *RXTE* ~1-yr light curve (Murphy et al. 2007) showed a very broad range of 2–10 keV flux levels for NGC 2992 (0.8–8.9 $\times 10^{-11}$ erg cm^{-2} s^{-1}). Our *Swift*-X-Ray Telescope (XRT) monitoring program is composed of 60 observations, ~2 ks long each, from 2019 March 26 to 2019 December 14. The source was targeted every 2 d during the *XMM–Newton* observing windows and every 4 d in the remaining months. The requested high flux threshold ($F_{2-10} > 7 \times 10^{-11}$ erg cm^{-2} s^{-1}) was met on 2019 May 6, with a 2–10 keV flux $F_{2-10} = 7.0 \pm 0.4 \times 10^{-11}$ erg cm^{-2} s^{-1}. The complete *Swift* observational campaign will be analysed in a separate paper (Middei et al., in preparation).

2.2 *XMM–Newton*

XMM–Newton started its observation of NGC 2992 on 2019 May 7 for two consecutive orbits (ObsIDs: 0840920201, 0840920301) with the European Photon Imaging Camera (EPIC) CCD cameras, the pn (Strüder et al. 2001) and the two MOS (Turner et al. 2001), operated in small window and medium filter mode. Data from the MOS detectors are not included in our analysis due to pile-up. The data from the pn camera show no significant pile-up as indicated by the EPATPLOT output. The extraction radii and the optimal time cuts for flaring particle background were computed with SAS 18 (Gabriel et al. 2004) via an iterative process that leads to a maximization of the signal-to-noise ratio (SNR), similar to the approach described in Piconcelli et al. (2004). The resulting optimal extraction radii for the source and the background spectra are 40

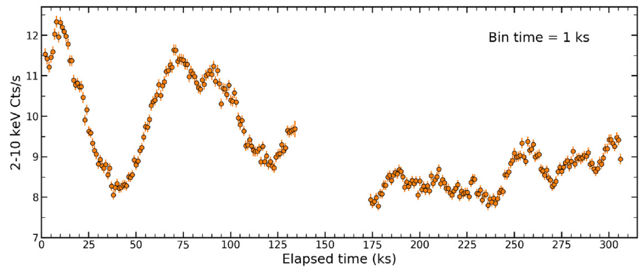

Figure 1. EPIC-pn light curve of the two consecutive observations of NGC 2992 in the 2–10 keV energy band.

and 50 arcsec, respectively. The net exposure times for the two time-averaged spectra are and 92.6 and 92.8 ks. We then decided to extract spectra from 5.8 ks time intervals during the *XMM–NuSTAR* simultaneous observations (191–301 ks from the beginning of the *XMM* pointing) and from 5 ks time intervals when *XMM* data alone are available. This choice allows us to have a regular time spacing that is centred on the *NuSTAR* on-source pointing. With this choice, we obtained 26 and 24 spectra for the first and second *XMM* orbits, respectively. Spectra were then binned in order to oversample the instrumental resolution by at least a factor of 3 and to have no less than 30 counts in each background-subtracted spectral channel, for the spectral fitting procedure. We adopt the cosmological parameters $H_0 = 70$ km s^{-1} Mpc^{-1}, $\Omega_\Lambda = 0.73$, and $\Omega_m = 0.27$, i.e. the default ones in XSPEC 12.10.1 (Arnaud 1996). Errors correspond to the 90 per cent confidence level for one interesting parameter ($\Delta\chi^2 = 2.7$), if not stated otherwise.

2.3 *NuSTAR*

NuSTAR (Harrison et al. 2013) observed NGC 2992 with its two co-aligned X-ray telescopes with corresponding Focal Plane Module A (FPMA) and Focal Plane Module B (FPMB) on 2019 May 10 for a total of ~119.2 ks of elapsed time. The Level 1 data products were processed with the *NuSTAR* Data Analysis Software (NUSTARDAS) package (v. 1.8.0). Cleaned event files (level 2 data products) were produced and calibrated using standard filtering criteria with the NUPIPELINE task and the latest calibration files available in the *NuSTAR* calibration data base (CALDB 20190410). Extraction radii for the source and background spectra were 60 and 70 arcsec and the net exposure times for the two time-averaged spectra are and 57.5 and 57.1 ks for the FPMA and FPMB, respectively. The two *NuSTAR* spectra were binned in order to oversample the instrumental resolution by at least a factor of 2.5 and to have a SNR greater than 3σ in each spectral channel, for the spectral fitting procedure. We then adopted a linear time sampling of 5.8 ks, for a total number of 20 pairs of spectra. The cross-calibration factors between the two detectors were found to be within 2 per cent in each time slice. A further constant was added (within 10 per cent throughout the observation), to consider *XMM–NuSTAR* cross-calibration uncertainties.

3 DATA ANALYSIS

3.1 Estimates of the black hole mass

The EPIC-pn light curves, extracted from the 2–10 keV energy band, are plotted in Fig. 1 and they show a count rate that ranges from 7.78 ± 0.11 to 12.33 ± 0.14 counts s^{-1}. They can be used

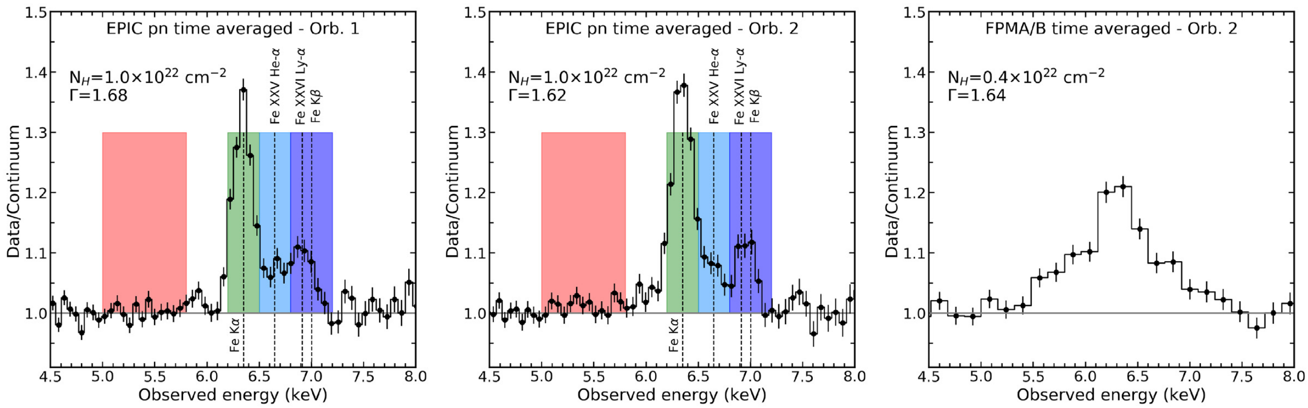

Figure 2. The ratios between the time-averaged data and the associated best-fitting continuum models are shown, for the EPIC-pn and FPMA/FPMB observations. The continuum is composed of an absorbed power law fitted between 3–5 plus 8–10 keV, the best-fitting values for the column density and photon index are reported in the top-left corner. The shaded regions indicate the four energy bands used for the variability patterns and the dashed lines show the emission lines between 6 and 7 keV included in the phenomenological spectral analysis.

to calculate a normalized excess variance $\sigma^2_{\rm rms} = 1.9 \pm 1.0 \times 10^{-3}$ (Nandra et al. 1997), adopting time bins of 250 s and selecting segments of 20 ks. Assuming the $\sigma^2_{\rm rms}$–$M_{\rm bh}$ correlation reported in Ponti et al. (2012), we estimate a black hole mass $M_{\rm BH} = (3.0^{+5.5}_{-1.5}) \times 10^7$ M$_\odot$, including also intrinsic uncertainties on the relation itself. The value obtained from the $M_{\rm BH}$–$\sigma_\star$ relation is $M_{\rm BH} = 4.8^{+3.9}_{-2.4} \times 10^7$ M$_\odot$), using a bulge stellar velocity dispersion $\sigma_\star = 158 \pm 13$ km s^{-1} (Nelson & Whittle 1995) and the relation from Gültekin et al. (2009). Given the good agreement between the $M_{\rm BH}$ inferred via the excess variance technique and the one derived from the $M_{\rm BH}$–$\sigma_\star$ relation, we will use a value of $M_{\rm BH} = 3.0^{+5.5}_{-1.5} \times 10^7$ M$_\odot$ for the black hole mass throughout the paper.

3.2 Time variability and excess maps

In the following, we will consider data in the 2–10 and 3–80 keV energy ranges for *XMM* and *NuSTAR* spectra. The detailed analysis of the broad-band data set will be the subject of a different paper (Marinucci et al., in preparation). We first fitted the time-averaged spectra with a model composed of an absorbed power law (ZWABS × POW in XSPEC) multiplied by a Galactic absorption component (TBABS) with $N_{\rm H} = 4.8 \times 10^{20}$ cm^{-2} (Kalberla et al. 2005), excluding the energy range dominated by the Fe K lines (5–8 keV). The ratios between the time-averaged data and the best-fitting continuum models are plotted in Fig. 2, once the 5–8 keV band is included. A cross-calibration constant is added to the FPMA/FPMB spectral fit and they are then simultaneously plotted using the SETPLOT GROUP command within XSPEC. The energy binning of the spectra is described in Section 2 and it is not the one used for creating the excess maps. Residuals are present on both the red and blue sides of the narrow iron Kα emission line, in all the three data sets. The main spectral changes are in the 5–6 and 6.5–7.2 keV bands, with clear variations between the first and the second *XMM* orbit.

We then applied this model for the continuum to each of the 50 spectral slices. *XMM* and *NuSTAR* spectra are fitted simultaneously when simultaneous data are available (time intervals between 191 and 301 ks), with the addition of a multiplicative constant to account for cross-calibration uncertainties. No residuals in excess to the best-fitting models are observed above 10 keV, suggesting a lack of a significant Compton hump due to cold reflection. Best-fitting models are stored and data with constant energy bins (100 eV for *XMM* and 200 eV for *NuSTAR*) are loaded. For each spectrum we calculate the excess of counts with respect to the corresponding model and plot it as a function of energy and time. Any appreciable intensity variations are expected to occur on longer time-scales than the sampling time (5–5.8 ks), therefore a smoothing procedure is expected to suppress the noise between adjacent pixels, providing a cleaner view of the possible variability patterns. Following the method described in Iwasawa et al. (2004) and Nardini et al. (2016), we smoothed the excess emission map through an elliptical Gaussian kernel with ($\sigma_{\rm E}$, $\sigma_{\rm t}$) = (1.06, 1.27) pixels for the first *XMM* orbit and ($\sigma_{\rm E}$, $\sigma_{\rm t}$) = (1.06, 1.10) pixels for the second one: corresponding to a full width at half-maximum (FWHM) of 250 eV × 15 ks. The different width in time $\sigma_{\rm t}$ is due to the larger time intervals (5.8 ks rather than 5 ks) adopted in the second *XMM* orbit. FPMA/FPMB detectors have a worse energy resolution (400 eV at 6 keV) than the EPIC-pn and we used ($\sigma_{\rm E}$, $\sigma_{\rm t}$) = (0.531, 1.10) pixels. For an energy binning of 200 eV and an integration time of 5.8 ks these values correspond to a FWHM of 250 eV × 15 ks. We plotted, in the four panels of Fig. 3, the energy-integrated count rates in excess to the continuum. We note that the energy bands of the smoothed data, due to the 250 eV width of the smoothing function, are wider than the ones used for the unsmoothed data. Counts integrated between 5 and 5.8 keV were associated with the *red flare*, between 6.2 and 6.5 keV to the narrow core of the iron Kα, between 6.5 and 6.8 keV to the *blue flare I*, and between 6.8 and 7.2 keV to the *blue flare II*. The different energy bands, overimposed to the time averaged spectra, can be seen in Fig. 2. Grey data points are used for plotting the excess count rates before the smoothing process in Fig. 3. We note that the smoothing process underestimates the 6.2–6.5 keV counts and overestimates the 6.5–6.8 keV counts (top panels in Fig. 3): this is an effect due to the 250 eV energy smoothing applied to the adjacent energy pixels. Assuming that the observed counts follow a Poissonian distribution ($\sigma_{\rm C} = \sqrt{C}$), we calculated their error bars as the root sum of the squares of the errors extrapolated from the best fits of the continuum and the ones on the counts in excess. For comparison, we find 3282 ± 57 counts for the continuum and 171 ± 13 counts in excess in the 5–5.8 keV band, in the 10 ks spectral slice. During the second orbit, at 278 ks, we obtain 2803 ± 53 and 184 ± 14 counts for the continuum and for the excess, respectively. When we apply the smoothing filter, we lose the counting statistics and we therefore run extensive simulations to estimate the error on the plotted ratios,

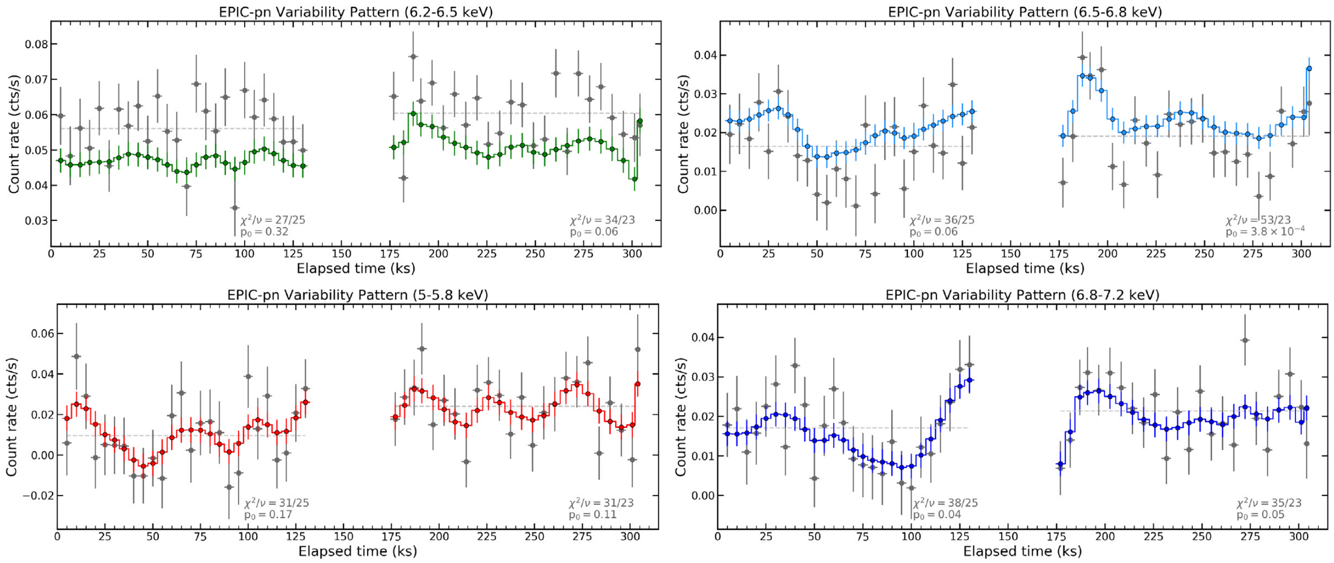

Figure 3. The smoothed excess count rates in the 6.2–6.5, 6.5–6.8, 5.0–5.8, and 6.8–7.2 keV bands are shown in green, light blue, red, and dark blue, respectively. Unsmoothed data are shown in grey. The best-fitting constant functions are shown as dashed grey lines.

as detailed below. Following the procedures presented in Iwasawa et al. (2004) and De Marco et al. (2009), we simulated $N_{\rm sim} = 1000$ time-energy maps with constant components in the four energy bands (obtained from fitting four Gaussians to the time-averaged spectra) with the associated best-fitting continuum model. Since the flux of the four spectral components (*red flare*, narrow iron Kα, *blue flare I*, and *blue flare II*) is fixed in each simulation, the variance of the individual light curves after the smoothing serves as the measurement uncertainty. We therefore considered the mean variance of the 1000 light curves and the standard deviation was assumed as the measurement error. To estimate the variability of the excess counts in the four energy bands, we applied a constant model to the unsmoothed data points and the corresponding χ^2/ν values and null-hypothesis probabilities p_0 are reported in Fig. 3. The largest deviation from a constant model is observed for the *blue flare I* component, during the second orbit.

At last, we added two narrow Gaussian components to reproduce the constant iron Kα/Kβ emission lines (with free energy and normalization for the former) to the *XMM*+*NuSTAR* continuum model and follow the previous steps to reproduce a count rate excess map. We will confirm in the next section that this spectral component is statistically consistent with being constant throughout the observation. The result is shown in Fig. 4. This is the first excess emission map constructed using *NuSTAR* data and, despite the lower spectral resolution and the non-consecutive on-source spectra, a flux modulation in the 5.5–6.5 keV band can still be observed. However, for these two reasons, we will only consider *XMM* data hereinafter.

3.3 $F_{\rm var}$ spectrum

Following Vaughan et al. (2003), we computed the fractional root mean square (rms) variability amplitude ($F_{\rm var}$; Ponti et al. 2004, 2006). To this aim we extracted light curves of each observation, in small energy bins (with a time bin of 50 s), and computed the Poisson noise subtracted power spectrum (normalized to units of squared fractional rms; Miyamoto et al. 1991). We integrated each power spectrum over the frequency range 0.9×10^5–10^4 Hz, corresponding to time-scales ranging between 110 ks (approximately covering the entire duration of a single observation) and 10 ks. These time-scales are chosen so as to sample the observed modulations in the Fe K line complex. From the square root of the integrated power we derived an estimate of the $F_{\rm var}$ as a function of energy, for each observation. Estimates from the two observations were then averaged to obtain the $F_{\rm var}$ spectrum displayed in Fig. 5. The $F_{\rm var}$ spectrum shows a spectral shape typical of absorbed sources (e.g. De Marco et al. 2020), with the soft energy drop due to the presence of constant spectral components that dominate this part of the spectrum. At higher energies (>1 keV) the $F_{\rm var}$ increases (∼7–9 per cent), with a peak at ∼2 keV and slightly decreasing towards harder energies. The sharp drop of $F_{\rm var}$ at $E \sim 6.4$ keV (marked by the vertical dashed line) is due to the presence of a constant neutral Fe Kα emission line. At slightly lower energies ($E \sim 5$–6 keV) the $F_{\rm var}$ shows instead an increase, which hints at presence of enhanced variability associated with redshifted Fe K line components. This result is in agreement with the behaviour observed in the excess map.

3.4 Spectral fitting

In the following, we describe the 2–10 keV spectral fitting of the 50 EPIC-pn spectra. Our aim is to characterize and explain the observed variability patterns around the Fe K complex, using both a phenomenological and a self-consistent physical model. We first model the counts excesses in the four energy bands shown in Fig. 3 with variable Gaussians and then with flaring spots from the accretion disc.

3.4.1 Phenomenological analysis

The phenomenological model applied to the data set is composed of the absorbed power law considered in Section 3.1 and five narrow Gaussian lines, to reproduce the neutral Fe Kα and Kβ, the Fe XXV Heα, and the Fe XXVI Lyα emission lines at 6.4, 7.058, 6.7, and 6.966 keV, respectively. One additional Gaussian is included in the model to reproduce the *red flare*. The normalization of the Fe Kβ line is fixed to $0.16 \times N_{\rm K\alpha}$ (Molendi, Bianchi & Matt 2003). The free parameters in the fits are the column density $N_{\rm H}$, the photon index

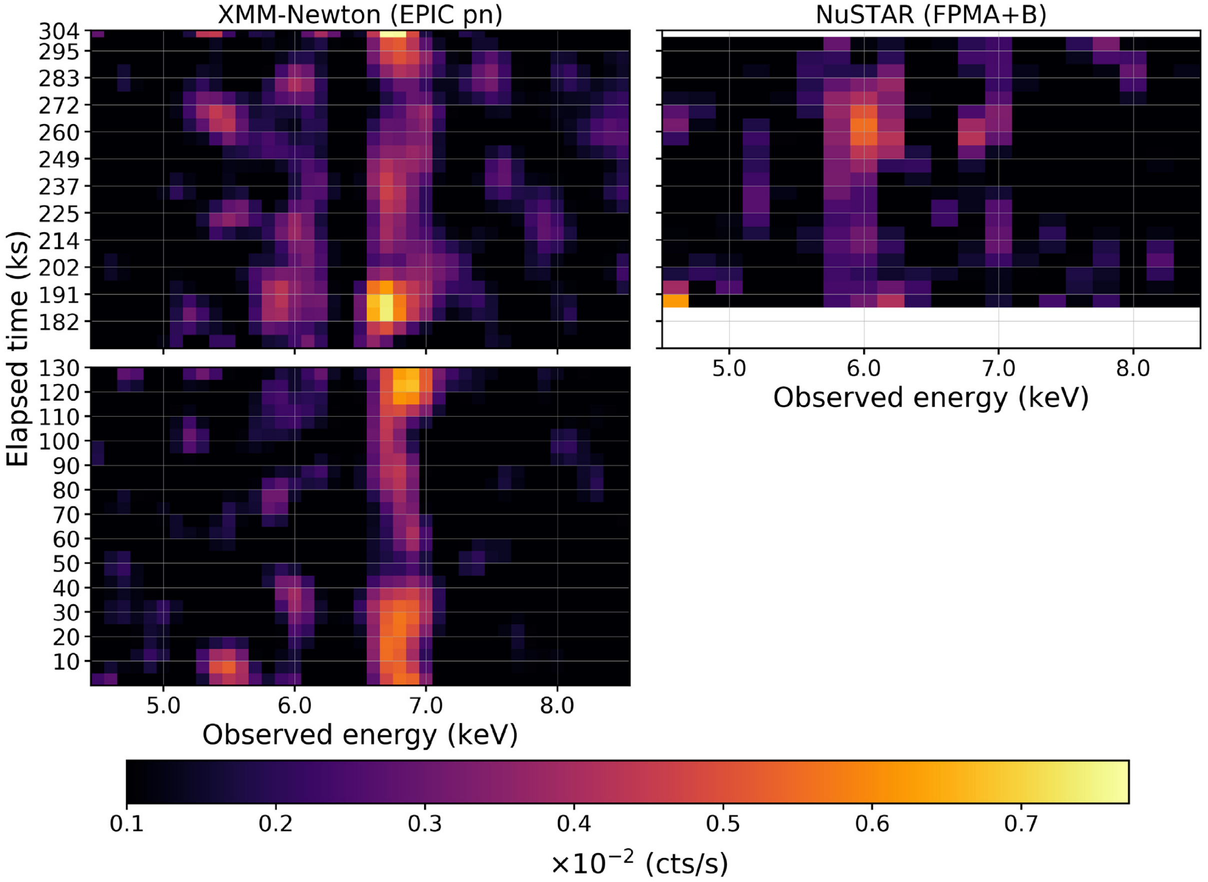

Figure 4. Excess emission map (in units of counts s^{-1}) for the full observation, when a model composed of a variable continuum and narrow iron Kα/Kβ emission lines at 6.4 and 7.058 keV are considered.

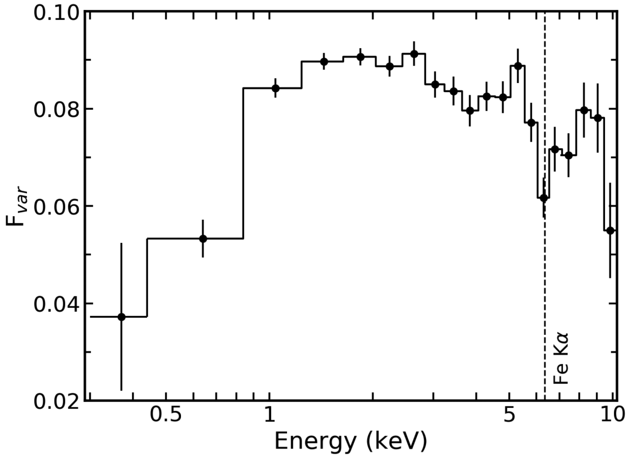

Figure 5. $F_{\rm var}$ spectrum of the full EPIC-pn observation. The dashed line indicates the neutral Fe Kα observed energy.

Γ, the energy centroid of the neutral Fe Kα, and the normalization of the power law of the four emission lines. The energy centroid of the spectral component associated with the *red flare* is fixed to 5.4 keV. We show the best-fitting values in Fig. 6, errors are calculated using a 68 per cent confidence level. The shaded regions indicate 1σ above and below the mean $N_{\rm H}$, Γ, energy centroid, and flux of the neutral iron Kα. The number of detected emission lines is reported in the top-centre of the three bottom panels. The minimum and maximum flux levels measured throughout the observation are $F_{2-10} = (6.8 \pm 0.1) \times 10^{-11}$ and $(1.01 \pm 0.01) \times 10^{-10}$ erg cm^{-2} s^{-1}, corresponding to luminosities $L_{2-10} = 9.5 \times 10^{42}$ and 1.5×10^{43} erg s^{-1} (corrected for intrinsic absorption), respectively. Adopting the bolometric correction $K_X(L_X)$ from Duras et al. (2020) and a black hole mass $M_{\rm BH} = 3 \times 10^7$ M$_\odot$, we obtain an accretion rate interval $L_{\rm Bol}/L_{\rm Edd} \simeq 4$–6 per cent.

While the neutral Fe Kα normalization is statistically consistent with being constant throughout the observation, variations of the other emission lines are detected. The maxima of the *red flare* normalization occur at 10 and 304 ks. For the sake of a visual comparison, we plot in the top panel of Fig. 7 the ratio between the data and the absorbed power-law model for the time-averaged spectrum (185.5 ks long) and for the two spectral slices corresponding to 10 and 50 ks, in which the maximum and an upper limit are retrieved for the *red flare* component. We show in the bottom panel of Fig. 7 the same ratios but for the maximum of the *blue flare I* component. The maxima of the Fe XXV Heα and Fe XXVI Lyα components occur at 187 and 40 ks, respectively. These values are in perfect agreement with our results from the excess map technique (Figs 3 and 4). The time-scales of the detected variations of the four phenomenological emission lines are consistent with distances of ~30–40$r_{\rm g}$ (for light-crossing times of 5–6 ks). This motivates the usage of a self-consistent model in which the transient Fe K lines are due to various orbiting flaring regions above the accretion disc.

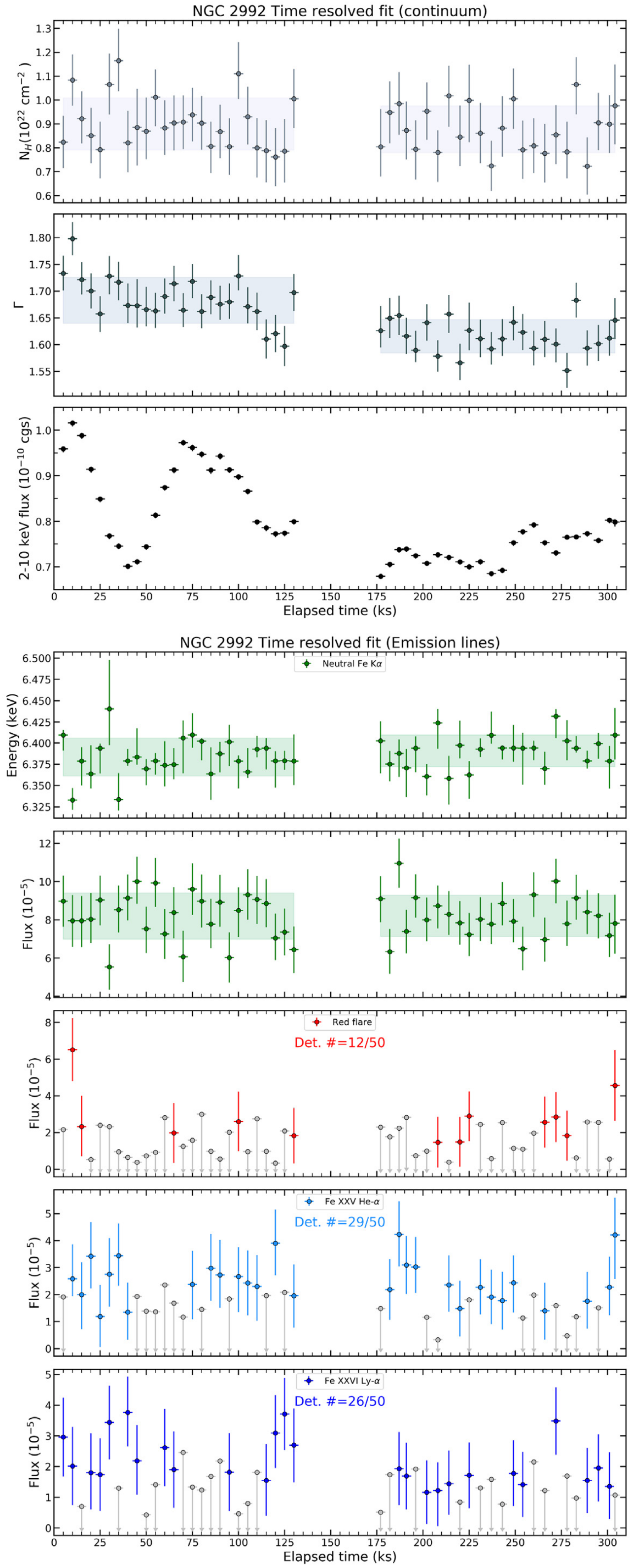

Figure 6. Best-fitting values for the continuum (top panels) and emission lines (bottom panels) when the phenomenological model described in Section 3.4.1 is applied to the *XMM* data set. Fluxes are in photons cm^{-2} s^{-1} units and shaded regions indicate 1σ above and below mean values. Errors are calculated using 68 per cent confidence level. The number of intervals in which the emission lines are detected is reported in the top centre of bottom panels.

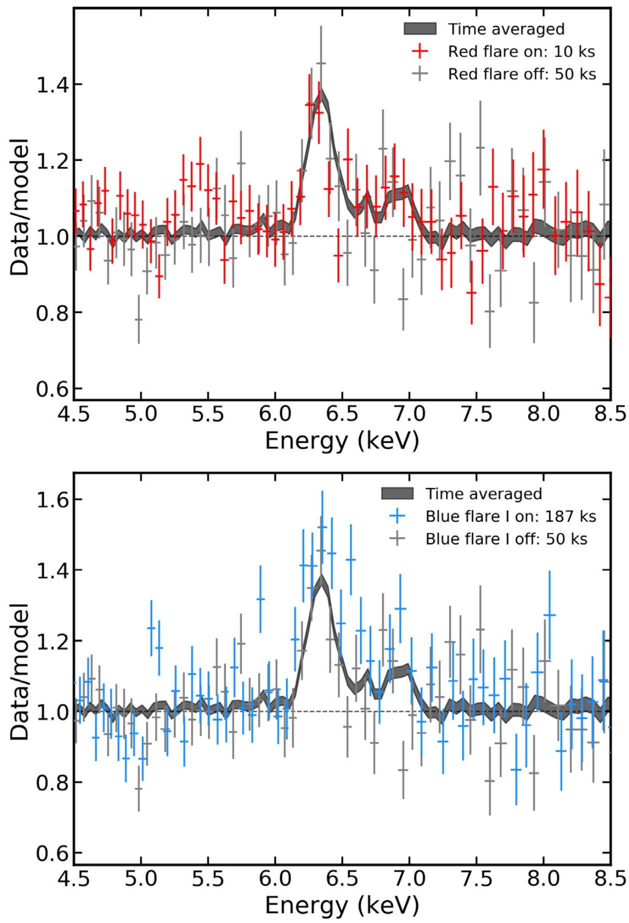

Figure 7. The ratios between the data and the absorbed power-law model are shown for the time-averaged spectrum (black shaded region) and for the two spectral slices corresponding to 10 ks (red data points, top panel), 187 ks (light blue data points, bottom panel), and 50 ks (grey data points), which are representative of the two flaring and one quiescent state.

3.4.2 The KYNRLINE model

In this section, we apply the KYN model (Dovčiak et al. 2004) to the 50 EPIC-pn spectra. The change of the emission lines amplitude and energy is explained in terms of orbital motion in a relativistic gravitational field close to the central black hole. The model assumes a space–time around the black hole that is described by the Kerr metric and a Keplerian, geometrically thin and optically thick accretion disc.[1] In particular, we use the KYNRLINE model component in XSPEC, which reproduces a relativistic line with a broken power-law radial emissivity. The emitting regions are non-axisymmetric, i.e. only part of the disc may be emitting (sections in radius and azimuth).

We first adopt a model that is composed of the absorbed power law considered in Section 3.1 and two narrow Gaussian lines, to reproduce the neutral Fe Kα and Kβ. The parameters Γ, $N_{\rm H}$, and normalization of the continuum are free. The Fe Kβ is always included in the following fits and its normalization is fixed to $0.16N_{\rm K\alpha}$. The neutral Fe Kα energy centroid and normalization are free. We then included a KYNRLINE component, fixing the

[1] A full description of the model can be found at https://projects.asu.cas.cz/stronggravity/kyn/.

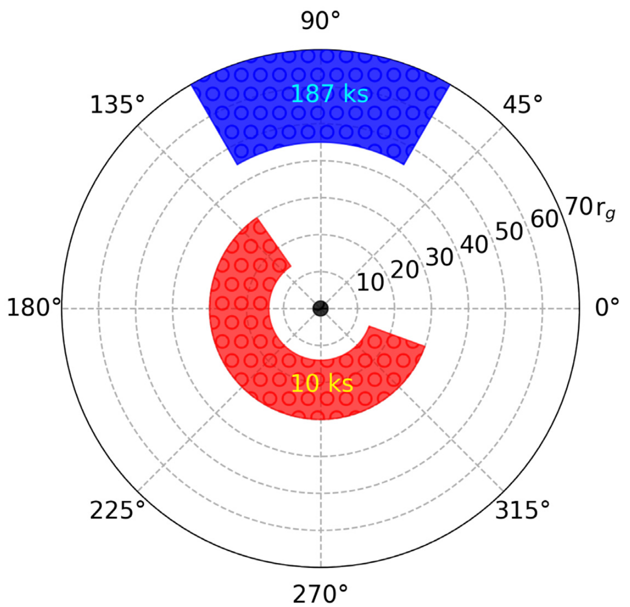

Figure 8. Schematic view of the emitting regions associated with the two KYNRLINE components described in Section 3.4.2. The red area indicates the best-fitting values that reproduce the *red flare* and the *blue flare II* at 10 ks, when the 5–5.8 keV excess is maximum. The blue one shows the best-fitting values for the *blue flare I* at its maximum, during the 187 ks time interval.

emissivity of the disc to $\epsilon(r) \propto r^{-3}$, the black hole spin to $a^* = 0.998$, and the annular region extension to $10r_g$. In our fits, we chose a framework where positive angular velocity corresponds to counterclockwise rotation and $\phi = 0°, 360°$ to the maximal Doppler blueshift for matter moving toward the observer (same convention as in Dovčiak et al. 2004; Nardini et al. 2016). We also assumed an energy at rest $E_R = 6.7$ keV and an inclination angle of the accretion disc $i = 40°$ with respect to our line of sight (Yaqoob et al. 2007). The properties of the emitting annuli are therefore estimated by leaving the inner radius r_{in}, the angle ϕ, and the angular extension $\Delta\phi$ free in the fits. For simplicity, the reported uncertainties on the angular sizes are the lower errors on ϕ and the upper errors on $\Delta\phi$. This first KYNRLINE spectral component reproduces the 5.4 and the 7.0 keV observed peaks (*red flare* + *blue flare II*). A second KYNRLINE component is then included in the model to account for the 6.7 keV excess (*blue flare I*).

This model is applied to the 50 EPIC-pn spectral slices. Best-fitting values for the primary continuum, neutral Fe Kα line, annular extension, size, and normalization of the KYNRLINE components are reported in Table A1. All the spectra, the corresponding best-fitting models, and the relative residuals are shown in Fig. A1. We plot in Fig. 8 a sketch of the emitting regions associated with the two KYNRLINE components for the 10 and 187 ks time intervals.

4 DISCUSSION

The EPIC-pn time variability patterns presented in Section 3.2 have shown several transient emission features throughout the 5–7 keV band and some recursive flares in the 5–5.8 keV band can be seen in Figs 3 and 4. If a sinusoidal function is applied to the unsmoothed data of the second *XMM* orbit (Fig. 3, bottom left-hand panel), a best-fitting orbital period $T = 41 \pm 1$ ks is retrieved, with a corresponding $\chi^2/\nu = 20/20$. Assuming a maximally rotating black hole spin and a black hole mass $M_{BH} = 3.0^{+5.5}_{-1.5} \times 10^7$ M$_\odot$, we can use the relation from Bardeen, Press & Teukolsky (1972) to estimate the radial distance r from the inferred orbital period T:

$$T = 310 \left[a + \left(\frac{r}{r_g} \right)^{\frac{3}{2}} \right] M_7 \text{ (s)},$$

$$r = \left[\frac{T}{310 \times M_7} - a \right]^{\frac{2}{3}} r_g = 12^{+8}_{-6} r_g, \quad (1)$$

where M_7 is the black hole mass in 10^7 M$_\odot$ units and a is the dimensionless back hole spin. The error bars on the radial distance r are dominated by the uncertainties on the black hole mass. We note, however, that Vaughan & Uttley (2008) observed that the detection of relativistically redshifted iron K lines could be the result of random fluctuations and Vaughan et al. (2016) estimated that at least five periodicities should be sampled to exclude a stochastic process effect.

To enhance the significance of the transient iron K lines, we co-added data extracted from time intervals with similar parameters of the continuum (i.e. column density, 2–10 keV flux and photon index) and in which the flares are most significant. We chose the time intervals peaking at 191, 225, 272, and 304 ks, for a total exposure time of 14.6 ks. We will call this co-added spectrum *flaring mode* spectrum (Fig. 9, left-hand panel).

When the KYNRLINE model described in the previous section is applied to the *flaring mode* spectrum, we retrieve a best-fitting $\chi^2/\nu = 135/137$, a best-fitting energy at rest $E_R = 6.7 \pm 0.1$ keV and an inclination angle of the accretion disc $i = 40° \pm 5°$ with respect to our line of sight, justifying our previous assumptions on these two parameters. The best-fitting values for the KYNRLINE component reproducing the *red flare* and *blue flare II* are $r_{in} = 15 \pm 3r_g$, $\phi = 165°$–$330°$, and $N = 11.5 \pm 3.5 \times 10^{-5}$ photons cm^{-2} s^{-1}. This spectral component well reproduces the 5.4 and 7.0 keV peaks and its very broad shape (red solid line in the right-hand panel of Fig. 9) is explained in terms of an emitting region close to a full ring of the accretion disc. The second KYNRLINE component (blue solid line in the right-hand panel of Fig. 9) is much narrower than the first one and the associated parameters are $r_{in} > 50r_g$, $\phi = 0°$–$120°$, and $N = 4.5 \pm 4.0 \times 10^{-6}$ photons cm^{-2} s^{-1}. The total best-fitting model is shown in Fig. 9 as a black solid line.

We show in Fig. 10 the contour plots between r_{in} and the normalization: a perfect agreement between r_{in} and the radial distance r retrieved from the periodicity of the *red flare* can be seen. Furthermore, the best-fitting values for the inclination angle of the accretion disc, the inner radius, and the normalization of the *red flare* + *blue flare II* component are perfectly consistent with the ones derived from previous high-flux *RXTE* and *XMM* observations (Murphy et al. 2007; Shu et al. 2010).

5 CONCLUSIONS

In the previous sections, we presented the analysis of the first simultaneous *XMM*+*NuSTAR* observations of NGC 2992 in an extremely bright state. The source is known to be intrinsically variable, up to a factor of 10 on time-scales of days, as observed during the past *RXTE* monitoring (Murphy et al. 2007). It was observed multiple times by *XMM–Newton* between 2010 and 2013, with a 2–10 keV flux always lower than $F_{2-10} < 1.7 \times 10^{-11}$ erg cm^{-2} s^{-1}. The only *XMM* observation of the source in the 2003 bright state was heavily affected by pile-up (Shu et al. 2010). Nevertheless, the authors found a relativistic iron Kα, in accordance with what already observed

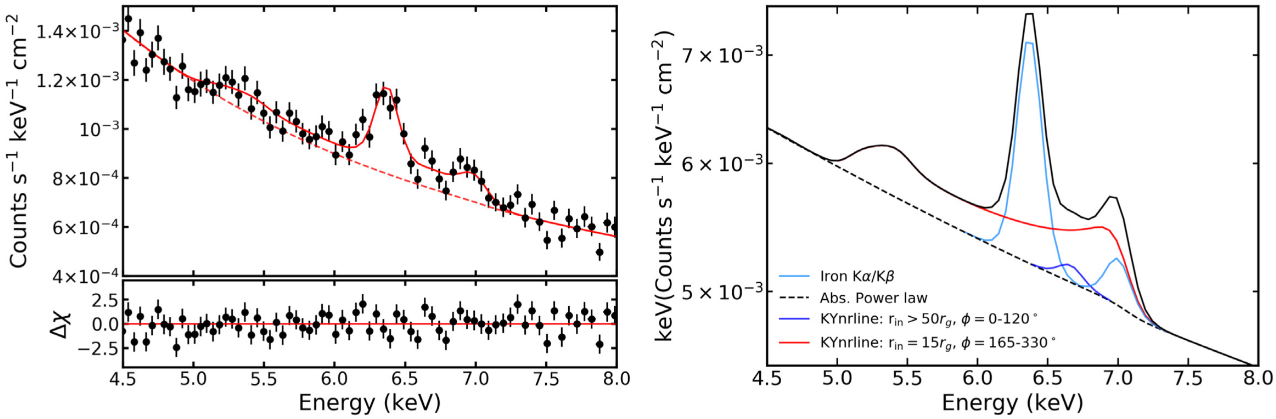

Figure 9. Left-hand panel: the *flaring mode* spectrum and the best-fitting model are plotted with the corresponding residuals. The spectrum is the sum of the ones extracted from time intervals peaking at 191, 225, 272, and 304 ks. Right-hand panel: the final KYNRLINE model applied to the 50 EPIC-pn spectra is shown in black, in the 4.5–8 keV band only. This represents the best-fitting model of the *flaring mode* spectrum only, the different components are free in each spectral slice. The dashed black line indicates the absorbed power-law component and the narrow iron Kα and Kβ emission lines are plotted in cyan. We show the *red flare* + *blue flare II* ($r_{\rm in} = 15 \pm 3r_{\rm g}$, $\phi = 165°$–$330°$) and *blue flare I* ($r_{\rm in} > 50r_{\rm g}$, $\phi = 0°$–$120°$) components as red and blue solid lines, respectively.

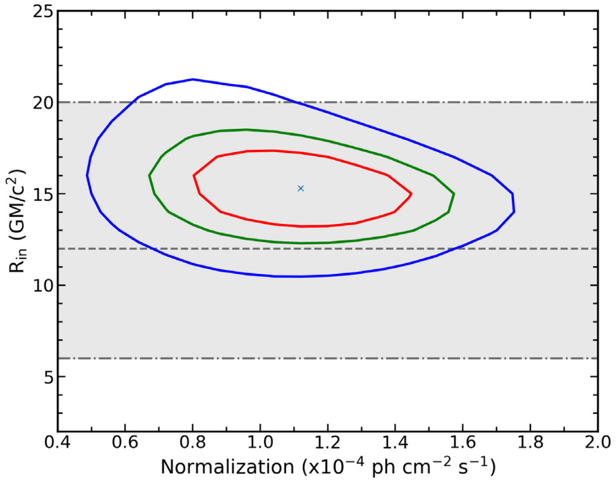

Figure 10. Contour plots between the inner radius of the annular region and the normalization of the *red flare* + *blue flare II* KYNRLINE component are shown, obtained from the best fit of the co-added spectra of NGC 2992 in the flaring state. Red, green, and blue solid lines indicate 68, 90, and 99 per cent confidence levels. The dashed and dotted–dashed black lines indicate the radial distance with its associated errors obtained from the periodicity of the *red flare* (see Section 3.2 for details).

with *RXTE*. To tackle the high flux levels of the source (i.e. $F_{2-10} > 7 \times 10^{-11}$ erg cm^{-2} s^{-1}), we obtained 60 *Swift*-XRT snapshots from 2019 March 26 to 2019 December 14 and the triggered *XMM–NuSTAR* observations started on 2019 May 7. We observe a range of fluxes corresponding to accretion rates $L_{\rm Bol}/L_{\rm Edd} \simeq 4$–6 per cent and we confirm the physical scenario in which the source exhibits strong redshifted/blueshifted Fe K lines at $L_{\rm Bol}/L_{\rm Edd} > 4$ per cent (Murphy et al. 2007; Marinucci et al. 2018).

From the *XMM–Newton* excess emission map shown in Section 3.2, we find hints of a recursive *red flare* at ∼5.4 keV, with a period $T = 41 \pm 1$ ks. For a maximally rotating black hole spin and considering the black hole mass of the source, the inferred period corresponds to a radial distance $r = 12^{+8}_{-6} r_{\rm g}$. A fully consistent value is found when the KYNRLINE model is applied to the co-added spectra of the flaring states only ($r_{\rm in} = 15 \pm 3r_{\rm g}$). We find that the *red flare* is likely associated with a second spectral component (*blue flare II*, at ∼7.0 keV) and can be modelled with a line-emitting annular region close to a full ring of the disc.

In the last few years, the technique of mapping the time variability of the flux in excess to the continuum, at different energies, has led to a number of results in bright AGN, with NGC 3516 (Iwasawa et al. 2004), Mrk 766 (Turner et al. 2006), NGC 3783 (Tombesi et al. 2007), and Ark 120 (Nardini et al. 2016) being the most significant ones. Differently from NGC 3516 and Mrk 766, we cannot constrain a clear evolution of the energy centroid of the emission lines, only changes in fluxes are detected. In our model, the *red flare* + *blue flare II* component likely arises from large angular regions close to the central black hole ($\phi \simeq 150°$–$360°$, $r_{\rm in} \simeq 10$–$40r_{\rm g}$), and well reproduces the excesses observed at 5–5.8 and 6.8–7.2 keV. The width of this sector is not due to the limited spectral quality of our data, but mainly by the necessity to account for both the red and most of the blue excess. On the other hand, the *blue flare I* component is much narrower and it is consistent with arising from smaller angular sectors, further away in the disc ($\phi \simeq 0°$–$150°$, $r_{\rm in} > 50r_{\rm g}$). The hotspot scenario (Ruszkowski 2000; Nayakshin & Kazanas 2001; Dovčiak et al. 2004) is often invoked to explain the observed variability of narrow iron Kα emission lines, both in energy and in flux. However, due to the lack of a significant shift in energy of the emission features observed and due to the large angular sectors that best reproduce the red component modulation, the hotspot picture seems unlikely. A single orbital spot cannot reproduce the whole variability patterns and the scenario seems much more complex. In particular, the periodicity of the *red flare* that is not observed in the *blue flare II* (bottom panels of Fig. 3) suggests that their angular distance cannot be resolved and only part of the angular sector is responsible for the periodical excess. Future X-ray observatories with higher spectral resolution and much larger effective area [such as *Athena*, *enhanced X-ray Timing and Polarimetry* (*eXTP*), *X-ray Imaging and Spectroscopy Mission* (*XRISM*)] will be crucial for this kind of studies.

ACKNOWLEDGEMENTS

We thank the anonymous referee for their suggestions that improved the paper. AM thanks A. De Rosa and M. Dovčiak for useful discussions. AM and RM acknowledge the support of the International Space Science Institute (ISSI Bern, Switzerland). BDM acknowledges support from the European Union's Horizon 2020 research and innovation programme under the Marie Skłodowska-Curie grant agreement no. 798726 and Polish National Science Center grant OPUS no. 2015/17/B/ST9/03422. We made use of ASTROPY,[2] a community-developed core PYTHON package for astronomy (Astropy Collaboration et al. 2013, 2018), and MATPLOTLIB (Hunter 2007). This research has made use of the *NuSTAR* Data Analysis Software (NUSTARDAS) jointly developed by the ASI Science Data Center (ASDC, Italy) and the California Institute of Technology (USA). EN acknowledges financial contribution from the agreement ASI-INAF n.2017-14-H.0 and partial support from the EU Horizon 2020 Marie Skłodowska-Curie grant agreement no. 664931.

REFERENCES

Arnaud K. A., 1996, in Jacoby G. H., Barnes J., eds, ASP Conf. Ser. Vol. 101, Astronomical Data Analysis Software and Systems V. Astron. Soc. Pac., San Francisco, p. 17

Astropy Collaboration et al., 2013, A&A, 558, A33

Astropy Collaboration et al., 2018, AJ, 156, 123

Bardeen J. M., Press W. H., Teukolsky S. A., 1972, ApJ, 178, 347

Bianchi S., Guainazzi M., Matt G., Fonseca Bonilla N., 2007, A&A, 467, L19

Chartas G., Kochanek C. S., Dai X., Poindexter S., Garmire G., 2009, ApJ, 693, 174

De Marco B., Iwasawa K., Cappi M., Dadina M., Tombesi F., Ponti G., Celotti A., Miniutti G., 2009, A&A, 507, 159

De Marco B., Ponti G., Cappi M., Dadina M., Uttley P., Cackett E. M., Fabian A. C., Miniutti G., 2013, MNRAS, 431, 2441

De Marco B. et al., 2020, A&A, 634, A65

Dovčiak M., Bianchi S., Guainazzi M., Karas V., Matt G., 2004, MNRAS, 350, 745

Duras F. et al., 2020, A&A, 636, A73

Fabian A. C., Vaughan S., 2003, MNRAS, 340, L28

Fabian A. C., Iwasawa K., Reynolds C. S., Young A. J., 2000, PASP, 112, 1145

Gabriel C. et al., 2004, in Ochsenbein F., Allen M. G., Egret D., eds, ASP Conf. Ser. Vol. 314, Astronomical Data Analysis Software and Systems (ADASS) XIII. Astron. Soc. Pac., San Francisco, p. 759

George I. M., Turner T. J., Yaqoob T., Netzer H., Laor A., Mushotzky R. F., Nandra K., Takahashi T., 2000, ApJ, 531, 52

Guerras E., Dai X., Steele S., Liu A., Kochanek C. S., Chartas G., Morgan C. W., Chen B., 2017, ApJ, 836, 206

Gültekin K. et al., 2009, ApJ, 698, 198

Harrison F. A. et al., 2013, ApJ, 770, 19

Hunter J. D., 2007, Comput. Sci. Eng., 9, 90

Iwasawa K., Fabian A. C., Young A. J., Inoue H., Matsumoto C., 1999, MNRAS, 306, L19

Iwasawa K., Miniutti G., Fabian A. C., 2004, MNRAS, 355, 1073

Kalberla P. M. W., Burton W. B., Hartmann D., Arnal E. M., Bajaja E., Morras R., Pöppel W. G. L., 2005, A&A, 440, 775

Kara E., Alston W. N., Fabian A. C., Cackett E. M., Uttley P., Reynolds C. S., Zoghbi A., 2016, MNRAS, 462, 511

Keel W. C., 1996, ApJS, 106, 27

Longinotti A. L., Nandra K., Petrucci P. O., O'Neill P. M., 2004, MNRAS, 355, 929

Marinucci A. et al., 2014, ApJ, 787, 83

Marinucci A., Bianchi S., Braito V., Matt G., Nardini E., Reeves J., 2018, MNRAS, 478, 5638

Martocchia A., Matt G., 1996, MNRAS, 282, L53

Miniutti G., Fabian A. C., 2004, MNRAS, 349, 1435

Miyamoto S., Kimura K., Kitamoto S., Dotani T., Ebisawa K., 1991, ApJ, 383, 784

Molendi S., Bianchi S., Matt G., 2003, MNRAS, 343, L1

Murphy K. D., Yaqoob T., Terashima Y., 2007, ApJ, 666, 96

Nandra K., George I. M., Mushotzky R. F., Turner T. J., Yaqoob T., 1997, ApJ, 477, 602

Nardini E., Porquet D., Reeves J. N., Braito V., Lobban A., Matt G., 2016, ApJ, 832, 45

Nayakshin S., Kazanas D., 2001, ApJ, 553, L141

Nelson C. H., Whittle M., 1995, ApJS, 99, 67

Parker M. L. et al., 2017a, MNRAS, 469, 1553

Parker M. L. et al., 2017b, Nature, 543, 83

Perola G. C., Matt G., Cappi M., Fiore F., Guainazzi M., Maraschi L., Petrucci P. O., Piro L., 2002, A&A, 389, 802

Petrucci P. O. et al., 2007, A&A, 470, 889

Piconcelli E., Jimenez-Bailón E., Guainazzi M., Schartel N., Rodríguez-Pascual P. M., Santos-Lleó M., 2004, MNRAS, 351, 161

Ponti G., Cappi M., Dadina M., Malaguti G., 2004, A&A, 417, 451

Ponti G., Miniutti G., Cappi M., Maraschi L., Fabian A. C., Iwasawa K., 2006, MNRAS, 368, 903

Ponti G., Papadakis I., Bianchi S., Guainazzi M., Matt G., Uttley P., Bonilla N. F., 2012, A&A, 542, A83

Reynolds C. S., Nowak M. A., 2003, Phys. Rep., 377, 389

Ruszkowski M., 2000, MNRAS, 315, 1

Shu X. W., Yaqoob T., Murphy K. D., Braito V., Wang J. X., Zheng W., 2010, ApJ, 713, 1256

Strüder L. et al., 2001, A&A, 365, L18

Tombesi F., De Marco B., Iwasawa K., Cappi M., Dadina M., Ponti G., Miniutti G., Palumbo G. G. C., 2007, A&A, 467, 1057

Trippe M. L., Crenshaw D. M., Deo R., Dietrich M., 2008, AJ, 135, 2048

Turner M. J. L. et al., 2001, A&A, 365, L27

Turner T. J., Miller L., George I. M., Reeves J. N., 2006, A&A, 445, 59

Uttley P., Cackett E. M., Fabian A. C., Kara E., Wilkins D. R., 2014, A&AR, 22, 72

Vaughan S., Uttley P., 2008, MNRAS, 390, 421

Vaughan S., Edelson R., Warwick R. S., Uttley P., 2003, MNRAS, 345, 1271

Vaughan S., Uttley P., Markowitz A. G., Huppenkothen D., Middleton M. J., Alston W. N., Scargle J. D., Farr W. M., 2016, MNRAS, 461, 3145

Yaqoob T. et al., 2007, PASJ, 59, 283

APPENDIX: BEST-FITTING RESULTS WITH KYNRLINE

We present in Table A1 the best-fitting parameters obtained with the KYNRLINE model described in Section 3.4.2. We show in Fig. A1 the spectra, the corresponding best-fitting models, and the relative residuals from the full *XMM–Newton* observation.

[2] http://www.astropy.org

Table A1. Best-fitting parameters of the time-resolved *XMM* analysis. Column densities are in cm^{-2}, energies are in keV, normalizations are in photons cm^{-2} s^{-1}, r_{in} are in r_g, and ϕ are in degrees. See Section 3.4.2 for details on the model.

Time	Best-fitting parameter										χ^2/ν
					Red flare + blue flare II			Blue flare I			
(ks)	N_H ($\times10^{22}$)	Γ	$E_{K\alpha}$	$N_{K\alpha}$ ($\times10^{-5}$)	r_{in}	ϕ	N_{RS} ($\times10^{-5}$)	r_{in}	ϕ	N_{BS} ($\times10^{-5}$)	
					Orbit 1						
5	0.82 ± 0.18	1.74 ± 0.05	6.41 ± 0.03	8.1 ± 2.2	20^{+40}_{-10}	180^{+160}_{-20}	9.0 ± 6.2	–	–	<1.7	114/113
10	1.08 ± 0.18	1.80 ± 0.05	$6.34^{+0.04}_{-0.01}$	6.3 ± 2.3	17 ± 3	140^{+200}_{-15}	14.7 ± 3.0	–	–	<2.8	116/115
15	0.93 ± 0.20	1.72 ± 0.05	6.38 ± 0.04	7.7 ± 2.3	–	–	<7.1	–	–	<3.9	126/117
20	0.82 ± 0.20	1.70 ± 0.05	$6.37^{+0.05}_{-0.03}$	7.0 ± 2.0	25^{+15}_{-5}	175^{+170}_{-20}	9.2 ± 6.3	–	–	<4.5	122/112
25	0.78 ± 0.19	1.65 ± 0.05	6.38 ± 0.02	9.0 ± 2.5	–	–	<6.7	–	–	<3.2	103/118
30	1.07 ± 0.21	1.74 ± 0.05	$6.37^{+0.06}_{-0.07}$	2.8 ± 2.8	45^{+20}_{-10}	180^{+190}_{-15}	10.7 ± 5.5	>80	100^{+20}_{-30}	2.8 ± 2.1	134/123
35	1.11 ± 0.23	1.71 ± 0.06	6.31 ± 0.07	5.5 ± 2.5	–	–	<7.0	30^{+30}_{-10}	60^{+80}_{-15}	8.2 ± 3.0	111/115
40	0.83 ± 0.23	1.68 ± 0.06	6.38 ± 0.03	7.5 ± 2.2	45^{+15}_{-10}	180^{+200}_{-20}	10.5 ± 5.0	–	–	<1.6	104/114
45	0.92 ± 0.22	1.68 ± 0.06	6.38 ± 0.04	8.7 ± 2.2	50^{+70}_{-30}	160^{+200}_{-160}	6.7 ± 4.3	–	–	<1.6	104/113
50	0.87 ± 0.19	1.66 ± 0.05	6.37 ± 0.03	7.6 ± 2.0	–	–	<4.6	–	–	<2.6	115/114
55	1.00 ± 0.21	1.66 ± 0.05	6.38 ± 0.03	9.8 ± 2.0	–	–	<4.4	–	–	<3.2	127/114
60	0.90 ± 0.19	1.69 ± 0.05	6.38 ± 0.05	6.3 ± 2.9	–	–	<8.5	140^{+30}_{-90}	30^{+60}_{-100}	2.8 ± 2.4	113/115
65	0.91 ± 0.18	1.72 ± 0.05	6.38 ± 0.03	8.1 ± 2.4	–	–	<10.2	–	–	<4.4	127/117
70	0.90 ± 0.18	1.66 ± 0.05	6.39 ± 0.05	6.1 ± 2.3	–	–	<9.5	–	–	<4.5	127/117
75	0.95 ± 0.18	1.72 ± 0.05	6.41 ± 0.03	9.5 ± 2.5	–	–	<10.3	180^{+20}_{-170}	50^{+60}_{-15}	2.7 ± 2.3	123/111
80	0.90 ± 0.20	1.66 ± 0.05	6.40 ± 0.03	9.0 ± 2.5	–	–	<5.3	–	–	<5.0	117/114
85	0.81 ± 0.18	1.69 ± 0.05	6.38 ± 0.05	5.7 ± 2.4	40^{+10}_{-5}	175^{+155}_{-15}	12.0 ± 5.3	–	–	<2.5	127/114
90	0.85 ± 0.18	1.68 ± 0.05	6.40 ± 0.07	5.3 ± 3.0	80^{+70}_{-35}	180^{+170}_{-20}	9.9 ± 5.0	–	–	<4.2	118/120
95	0.90 ± 0.19	1.69 ± 0.06	6.41 ± 0.04	6.4 ± 2.1	–	–	<6.0	–	–	<2.7	100/119
100	1.15 ± 0.20	1.74 ± 0.05	6.38 ± 0.03	8.1 ± 2.2	–	–	<7.7	–	–	<3.5	121/117
105	0.94 ± 0.20	1.67 ± 0.06	6.38 ± 0.03	9.3 ± 2.3	–	–	<6.7	–	–	<4.4	121/116
110	0.81 ± 0.20	1.67 ± 0.06	6.40 ± 0.03	8.4 ± 2.3	–	–	<11.5	–	–	<3.8	102/115
115	0.77 ± 0.21	1.60 ± 0.06	6.39 ± 0.03	8.7 ± 2.3	–	–	<8.2	–	–	<4.0	114/114
120	0.76 ± 0.20	1.62 ± 0.06	6.38 ± 0.04	6.0 ± 2.5	35^{+25}_{-15}	180^{+200}_{-20}	9.2 ± 5.6	150^{+50}_{-120}	60^{+70}_{-40}	2.8 ± 2.3	129/111
125	0.80 ± 0.21	1.60 ± 0.06	6.38 ± 0.04	6.2 ± 2.5	30^{+5}_{-10}	180^{+300}_{-30}	9.4 ± 5.1	–	–	<4.2	132/114
130	1.00 ± 0.20	1.71 ± 0.06	6.38 ± 0.04	6.2 ± 2.5	10^{+5}_{-3}	180^{+200}_{-20}	16.0 ± 8.4	–	–	<2.9	124/114
					Orbit 2						
177	0.81 ± 0.23	$1.63^{+0.07}_{-0.06}$	6.40 ± 0.03	8.7 ± 2.0	–	–	<7.6	–	–	<1.2	108/110
182	0.92 ± 0.21	1.64 ± 0.06	$6.38^{+0.04}_{-0.03}$	6.1 ± 2.0	–	–	<5.7	>150	30^{+100}_{-40}	2.6 ± 2.0	127/111
187	$0.98^{+0.20}_{-0.32}$	$1.67^{+0.08}_{-0.09}$	$6.33^{+0.05}_{-0.03}$	7.3 ± 2.2	43^{+15}_{-32}	170^{+250}_{-40}	7.7 ± 4.5	>45	70^{+50}_{-10}	7.7 ± 2.5	127/108
191	0.86 ± 0.25	$1.63^{+0.06}_{-0.05}$	6.31 ± 0.05	5.0 ± 2.1	14^{+5}_{-7}	180^{+180}_{-15}	11.5 ± 4.7	>400	100^{+240}_{-50}	4.7 ± 2.0	112/110
196	0.78 ± 0.25	1.59 ± 0.06	6.37 ± 0.03	7.9 ± 1.8	–	–	<9.6	>350	80^{+250}_{-25}	5.4 ± 2.2	94/112
202	0.98 ± 0.20	1.65 ± 0.05	6.36 ± 0.03	$7.4^{+1.8}_{-2.0}$	28^{+10}_{-8}	120^{+280}_{-30}	8.4 ± 2.5	–	–	<2.5	130/111
208	0.81 ± 0.20	1.59 ± 0.06	6.39 ± 0.05	7.6 ± 2.5	–	–	<6.9	–	–	<4.6	110/115
214	1.03 ± 0.22	1.67 ± 0.07	6.37 ± 0.05	5.5 ± 2.5	70^{+70}_{-45}	180^{+250}_{-30}	6.2 ± 3.2	50^{+200}_{-35}	65^{+150}_{-25}	3.2 ± 2.7	85/109
220	0.86 ± 0.22	1.57 ± 0.06	6.41 ± 0.03	7.5 ± 2.0	–	–	<8.2	–	–	<2.9	103/113
225	1.02 ± 0.20	1.65 ± 0.05	6.35 ± 0.05	6.0 ± 2.0	18^{+5}_{-3}	160^{+190}_{-15}	11.6 ± 5.1	–	–	<2.3	107/127
231	0.86 ± 0.21	1.62 ± 0.06	6.39 ± 0.04	7.1 ± 1.9	20^{+25}_{-15}	165^{+180}_{-20}	6.0 ± 4.8	–	–	<3.1	133/111
237	0.73 ± 0.20	1.60 ± 0.06	6.41 ± 0.05	5.8 ± 2.4	–	–	<3.6	20^{+30}_{-5}	45^{+25}_{-15}	$6.1^{+3.0}_{-4.1}$	114/110
243	0.89 ± 0.21	1.62 ± 0.06	6.38 ± 0.04	7.2 ± 2.3	–	–	<9.0	–	–	<6.0	142/113
249	1.00 ± 0.21	1.65 ± 0.06	6.39 ± 0.03	7.3 ± 2.0	–	–	<9.5	>50	60^{+180}_{-60}	2.6 ± 2.2	114/111
254	0.80 ± 0.20	1.63 ± 0.07	6.39 ± 0.03	6.0 ± 2.0	30^{+15}_{-10}	130^{+220}_{-40}	4.8 ± 3.4	–	–	<3.6	98/113
260	0.81 ± 0.19	1.59 ± 0.06	6.39 ± 0.03	8.8 ± 2.1	–	–	<9.0	–	–	<3.5	113/118
266	0.78 ± 0.21	1.62 ± 0.06	6.36 ± 0.04	6.2 ± 2.0	17^{+8}_{-10}	160^{+180}_{-40}	6.2 ± 5.2	–	–	<2.5	117/112
272	0.86 ± 0.21	1.61 ± 0.06	6.42 ± 0.04	8.9 ± 2.0	15^{+4}_{-6}	160^{+200}_{-15}	12.9 ± 5.8	–	–	<2.0	85/113
278	0.80 ± 0.18	1.56 ± 0.06	6.40 ± 0.02	7.5 ± 2.0	–	–	<7.2	–	–	<2.5	106/116
283	0.88 ± 0.20	1.68 ± 0.05	6.39 ± 0.03	9.0 ± 2.0	–	–	<7.2	–	–	<2.5	121/116
289	0.73 ± 0.20	1.60 ± 0.05	6.38 ± 0.02	8.0 ± 2.0	–	–	<9.8	>180	20^{+50}_{-80}	2.2 ± 2.0	119/111
295	0.91 ± 0.20	1.60 ± 0.06	6.40 ± 0.03	8.0 ± 2.0	–	–	<8.8	–	–	<3.0	121/116
301	0.89 ± 0.20	1.61 ± 0.06	6.36 ± 0.04	5.8 ± 2.1	–	–	<9.2	30^{+120}_{-15}	40^{+70}_{-10}	4.4 ± 3.2	87/112
304	1.06 ± 0.30	1.68 ± 0.08	6.43 ± 0.05	6.9 ± 2.7	15^{+5}_{-5}	130^{+270}_{-40}	11.7 ± 8.0	>200	50^{+100}_{-40}	3.2 ± 2.5	102/102

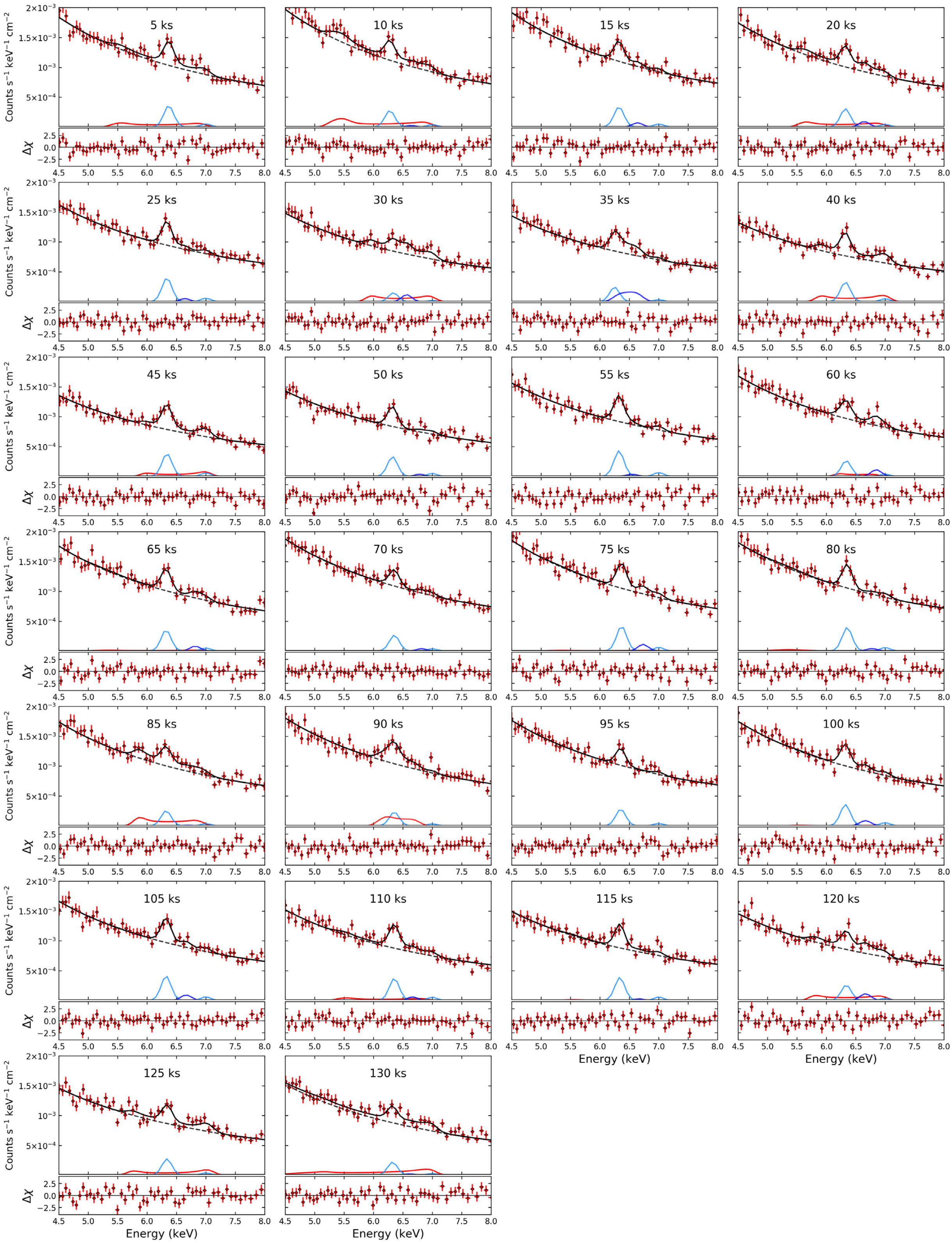

Figure A1. *XMM* EPIC-pn data (divided by the instrumental effective area), best fits, and residuals are shown, in the 4.5–8.0 keV band. Black solid lines indicate best-fitting models, dashed black lines indicate the power-law spectral component, cyan solid lines indicate best-fitting iron Kα and Kβ components, red and blue solid lines indicate the two KYNRLINE components (*red flare* + *blue flare II* and *blue flare I*).

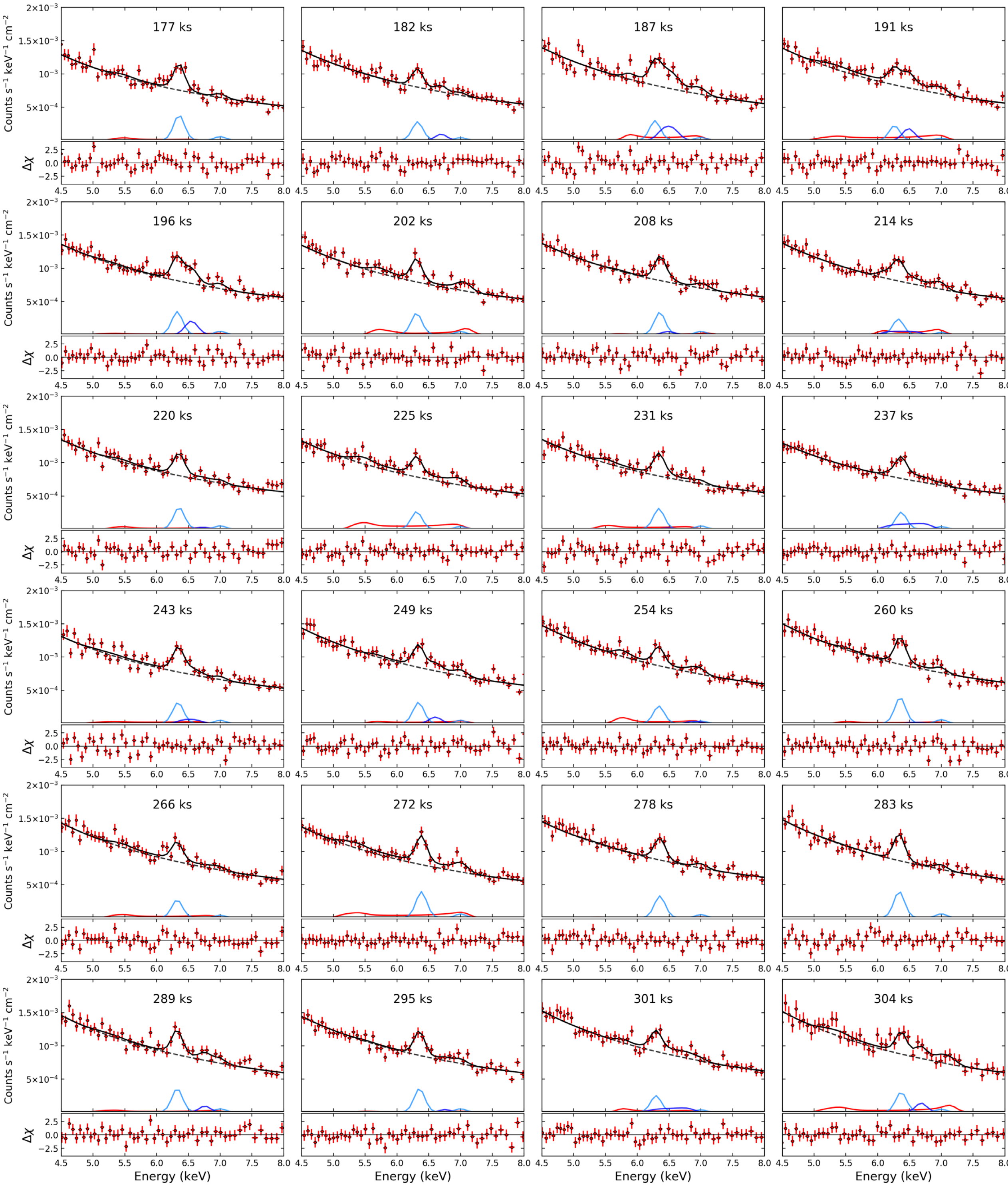

Figure A1 – *continued.*

This paper has been typeset from a TEX/LATEX file prepared by the author.